Time-Resolved High Dynamic Range PIV using Local Uncertainty Estimation

Tim Persoons[1]

University of Dublin, Trinity College, Dublin, 2, Ireland

The dynamic velocity range of particle image velocimetry (PIV) is the ratio of maximum to minimum resolvable displacement. Although many techniques have been developed in recent years to extend the dynamic range, flows with a wide velocity range still challenge conventional PIV. Using multiple-pulse-separation acquisition and a new criterion for the local optimal pulse separation, this paper presents a novel time-resolved high dynamic range (HDR) PIV methodology. The algorithm maximizes a vector quality metric combining correlation peak ratio with the estimated local displacement uncertainty and magnitude, expressed as a modified signal-to-noise ratio. Using an axisymmetric turbulent jet as a benchmark case, significant enhancements are shown in the measured turbulence intensity and signal-to-noise ratio throughout the flow field, but especially in the entrainment region and the outer shear layer. For this case, HDR PIV increases the dynamic velocity range by 16.5x compared to conventional double-frame PIV. Hot-wire anemometry is used in characteristic flow field locations as a reference measurement. The results show that time-resolved HDR PIV automatically selects the optimal pulse separation in each location as a function of time. The method relies only on readily available data, has a low computational cost and is fully compatible with conventional multi-grid vector evaluation algorithms.

---

[1] Ussher Assistant Professor in Engineering, AIAA Member

School of Engineering, Department of Mechanical and Manufacturing Engineering, Parsons Building, Trinity College Dublin (Tel.: +353 1 896 1936, Fax: +353 1 679 5554, E-mail: tim.persoons@tcd.ie).

Nomenclature

D	=	jet nozzle diameter, m
d_I	=	interrogation window size, pixel
DR_V	=	dynamic velocity range
δt	=	time step (i.e., inverse of camera frame rate), s
G	=	displacement vector quality metric ($G = Q\left(s_{mag}/\Delta s\right)^m$)
k_g	=	grid refinement factor
k_τ	=	maximum to minimum pulse separation ratio
M	=	optical scaling factor, m/pixel
m	=	exponent in expression for vector quality metric G (Eq. (2))
N_τ	=	number of pulse separation values used in HDR algorithm
n_x, n_y, n_t	=	number of elements (in x, y, t direction) in uncertainty estimation kernel
Q	=	ratio of highest to second highest peak in correlation space
Re	=	jet Reynolds number
r	=	radial coordinate in axisymmetric jet, m
s	=	particle image displacement, pixel
s_{mag}	=	local displacement magnitude, pixel
t	=	time, s
U_{jet}	=	spatially averaged velocity in jet nozzle, m/s
U, V	=	velocity components, m/s
x, y	=	spatial coordinates in measurement plane, m
β_s	=	displacement bias error, pixel
Δs	=	total error or estimated uncertainty of displacement, pixel
ϵ_s	=	displacement random error, pixel
σ	=	minimum resolvable quantity
τ	=	pulse separation time, s

Subscripts

s	=	particle image displacement
V	=	velocity

I. Introduction

THE dynamic velocity range of particle image velocimetry (PIV), DR_V, is defined as the ratio of maximum to minimum resolvable velocity, or $DR_V = V_{max}/\sigma_V = s_{max}/\sigma_s$, where σ_V and σ_s are the minimum resolvable velocity and particle displacement, respectively ($\sigma_V = M\sigma_s/\tau$, where M is the spatial pixel resolution and τ is the pulse separation time). The minimum resolvable displacement σ_s is determined by the overall displacement error comprising both random and bias error, i.e. $\sigma_s = \lim_{s\to 0}(\Delta s)$, where $\Delta s = \sqrt{\epsilon_s^2 + \beta_s^2}$. It is assumed that the errors are evaluated at near zero displacement when using multi-pass correlation.

Various techniques have been developed to extend the dynamic range by increasing the maximum or reducing the minimum measurable displacement. For single-pass correlation algorithms, Keane and Adrian [1, 2] proposed the quarter window rule ($s_{max} < \frac{1}{4}d_I$) to avoid excessive loss of correlation strength due to in-plane displacement, yielding $DR_V^{(SP)} = \frac{1}{4}d_I/\sigma_s^{(SP)}$. The dependence of $\sigma_s^{(SP)}$ on a large number of parameters (e.g., particle image displacement, density and diameter, interrogation window size, image noise, digitization and quantization, velocity gradients) has been reviewed extensively for single-pass correlation [3-6].

Using iterative window deformation with progressive grid refinement (multi-grid correlation), a tenfold reduction in uncertainty is achieved compared to single-pass correlation, with $\sigma_s^{(MG)} \cong 0.001$ pixel based on an analysis of Monte Carlo simulations of noiseless artificial particle images [7-9]. Multi-grid techniques partly decouple the maximum displacement and final interrogation window size, since the quarter rule [3] only applies to the first, coarse grid and not to subsequent passes. With an initial interrogation window size $k_g d_I$ and a final size d_I (where typically k_g = 2-4), the dynamic range becomes $DR_V^{(MP)} = \frac{1}{4}k_g d_I/\sigma_s^{(MP)}$.

However, in realistic laboratory conditions, image noise and velocity gradients yield much larger uncertainty values than in artificial images, with typical values of $\sigma_s^{(MG)}$ around 0.1 pixel [10]. Despite the use of advanced evaluation algorithms, a realistic dynamic velocity range for multi-grid PIV is therefore of the order of $DR_V \cong 160{:}1$ (for $k_g = 4$, $d_I = 16$ pixel). In a recent review, Westerweel et al. [11] note that current double-pulsed PIV systems are limited to about $DR_V \cong 200{:}1$, and that a key objective for the next few years is to increase this dynamic velocity range to 1,000:1. One possible new method discussed by Westerweel et al. [11] is triple-pulse PTV/PIV, in which information from a third laser pulse is used to determine the local fluid acceleration. Based on a sensitivity analysis, the authors propose a pulse separation time ratio of about 3:1 between these three pulses to yield the best results in terms of particle tracking velocimetry (PTV) velocity accuracy. However, extending this approach to correlation-based PIV is more computationally intensive and further work is needed to achieve this.

For double-pulsed PIV, Adrian [12] noted that the product of dynamic spatial range and dynamic velocity range is constant for a given system, where the dynamic spatial range is the ratio of image sensor size to the maximum allowable particle image displacement. By globally changing the pulse separation time, a high spatial resolution (i.e., small particle displacement compared to the image sensor size) can only be achieved by sacrificing accuracy and dynamic velocity range, and vice versa. This provides an inherent limitation to traditional double-pulsed PIV where only one global pulse separation time can be set. However as discussed next, some approaches rely on locally varying the pulse separation time.

By locally adapting the pulse separation time, some methods have attempted to partially decouple the dynamic spatial range and dynamic velocity range, which allows for an improvement of the dynamic velocity range over conventional double-pulsed PIV for the same dynamic spatial range. Hain and Kähler [13] proposed an iterative, time-resolved multi-frame technique to compensate for the loss in dynamic range of CMOS sensors used in high speed PIV systems. This method selects at each location a pair of images within the sequence such that the particle image displacement is maintained approximately uniform (e.g. 10 pixels). In this case, the choice of optimal time separation is crucial. Multi-frame (MF) PIV has achieved good results compared to conventional PIV in low speed flows with a wide velocity range [13-15].

An alternative multi-frame approach for time-resolved PIV was proposed by Sciacchitano et al. [16] using a linear combination of the correlation map obtained at different pulse separation time intervals, resulting in an ensemble-averaged correlation map with a higher signal-to-noise ratio. This so-called pyramid correlation technique has been shown to yield an order of magnitude improvement in the velocity estimation precision, based on an analysis using artificial particle images. Lynch and Scarano [17] have extended conventional particle tracking velocimetry by tracking a patterned fluid element across multiple frames; this reduces the relative velocity error by enlarging the measurement interval as well as allowing for more accurate nonlinear fitting. An increase in dynamic velocity range in excess of one order of magnitude is observed for experimental validation experiments using an axisymmetric jet flow.

The aforementioned techniques [13-17] rely on single-frame/single-exposure imaging. By contrast, some other techniques increase the dynamic velocity range by directly combining information obtained from cross-correlating double-frame/single-exposure images obtained at different pulse separation times [18, 19]. The multi-pulse separation (MPS) technique applies a greater pulse separation in regions of the flow field where the displacement magnitude would otherwise be of the order of the minimum resolvable displacement σ_s. This is analogous to high dynamic range (HDR) photography, which generates a composite image based on the weighted sum of a set of images taken at different exposure times [20-22]. Unlike linear superposition used in HDR photography, the MPS PIV algorithm determines a local optimum pulse separation by a criterion balancing correlation strength and measurement uncertainty. The reconstruction is nonlinear to avoid the propagation of spurious vectors resulting from the evaluation of images taken at an excessive pulse separation [18].

Using a constant value for the estimated displacement uncertainty (σ_s = 0.1 pixel), a significant improvement in the phase-averaged mean flow and turbulence intensity in an impinging synthetic jet flow was observed by [19] compared to conventional PIV. However, to extend the technique to time-resolved flows, a method for determining the local uncertainty was needed, as will be described further in this paper.

In order to implement advanced PIV techniques, different methods for estimating the local uncertainty $\Delta s = \sqrt{\epsilon_s^2 + \beta_s^2}$ have been evaluated. Previous estimates could only provide guidance on the expected error for an average measurement under specific image quality and flow conditions, but recent advancements have been made in the field of PIV uncertainty. Wilson and Smith [23] compared PIV velocity fields to the known particle displacement for a rectangular jet flow. For a specific combination of four parameters (displacement, shear, particle image density and particle image diameter), Timmins et al. [24] determined the four-dimensional uncertainty response, termed the "uncertainty surface". Flow gradients, large particle images and insufficient particle image displacements resulted in elevated measurements of turbulence levels.

Charonko and Vlachos [25] developed a method for measuring error bounds to within a given confidence interval for a specific, individual measurement. The authors found that a strong correlation exists between the observed error and the correlation peak ratio Q (i.e., the ratio of the height of the first peak to the second in the spatial correlation domain). This correlation was found to hold regardless of flow condition and image quality.

Xue *et al.* [26] posited that the signal-to-noise-ratio (SNR) metrics calculated from the PIV correlation plane can be used to quantify the quality of correlation, and subsequently the uncertainty of an individual measurement. The relationship between SNR and uncertainty was explored for both the robust phase correlation (RPC) and standard cross correlation (SCC) processing. In the correlation metric, the uncertainty was a function of three terms: A Gaussian function used to account for uncertainty due to invalid measurements, a power-law term that describes the contribution of valid vectors to uncertainty, and a constant expressing the minimum achievable uncertainty.

Sciacchitano et al. [27] proposed a method for estimating uncertainty and bias error inspired by super-resolution PIV, relying only on statistical analysis of the particle disparity vector field from the residual distance between matched image pairs. The approach is validated using a Monte Carlo analysis with artificial particle images and further demonstrated using experimental time-resolved PIV data of a submerged turbulent water jet at *Re* = 5000, using the pyramid correlation technique [16] as a reference measurement.

In this paper, the multiple-pulse-separation (MPS) PIV technique is extended towards time-resolved flows, using an axisymmetric unconfined turbulent jet flow as a benchmark case (similar to Sciacchitano et al. [27]) and hot wire anemometry as a reference velocity measurement. Compared to earlier studies for *non*-time-resolved multiple pulse separation PIV [18, 19] valid only for steady and periodic flows, the current paper presents a new more general criterion for the local optimal pulse separation, based on the estimated local particle displacement uncertainty.

II. Methodology: Time-Resolved HDR PIV with Local Uncertainty Estimation

Persoons and O'Donovan [18] proposed the multiple-pulse-separation (MPS) technique to achieve high dynamic range (HDR) PIV results for steady or ensemble-averaged periodic flows with phase-locked acquisition. The current paper presents a more general MPS methodology to extend this approach to time-resolved flows. Whereas multi-frame techniques [13-17] acquire single-frame image sequences $\{\dots, t, t+\delta t, t+2\delta t, \dots\}$, MPS PIV uses a customised timing system to acquire double-frame images $\{\dots, [t, t+k_{\tau,1}\tau_{min}], [t+\delta t, t+\delta t+k_{\tau,2}\tau_{min}], \dots\}$ with successive different pulse separation values $k_{\tau,i}\tau_{min}$ ($1 \le i \le N_\tau$) at a given frame rate $1/\delta t$. Each image pair $[I(t), I(t+\tau_i)]$ with pulse separation $\tau_i = k_{\tau,i}\tau_{min}$ is correlated using conventional multi-grid algorithms resulting in the displacement fields $\vec{s}_i = \vec{s}(x, y, t, \tau_i)$.

In its simplest implementation using a conventional timing system, two pulse separation values can be included in the MPS algorithm by combining the information from $[I(t), I(t+\tau_{min})]$ (as double-frame cross-correlation) and $[I(t), I(t+\delta t)]$ (as time-series cross-correlation), where $\tau_1 = \tau_{min}$ and $\tau_2 = \tau_{max} = \delta t$ (and $N_\tau = 2$). This simple approach is used in this paper. Its implications are discussed in Section IV.C, along with the main limitations of the technique.

To determine the optimum pulse separation $\tau_{opt}(x, y)$ for each location in a time- or phase-averaged flow, Persoons and O'Donovan [18] maximized the time-averaged product of the correlation peak ratio Q and a measure of the displacement precision, thereby balancing correlation strength and precision:

$$Q'(x, y, \tau) = \overline{Q(x, y, t, \tau)\left(1 - \frac{\sigma_s}{s_{mag}(x,y,t,\tau)}\right)} \tag{1}$$

where the displacement magnitude $s_{mag} = \tau\sqrt{U^2 + V^2}/M$. At each location (x, y), the maximum of $Q'(x, y, \tau_i)$ determines the local optimum pulse separation. This method assumed a constant minimum resolvable displacement value $\sigma_s(\approx \Delta s) = 0.1$ pixel. This order of magnitude seemed appropriate for multi-grid algorithms in realistic conditions, based on validation results in the review of Stanislas *et al*. [10].

However, assuming a global constant displacement uncertainty is not a valid approach for time-resolved PIV, wherein Δs can vary significantly with respect to location and time. In this constant uncertainty approach, for each spatial location only one suitable pulse separation would be selected, thus the algorithm would not adapt to time-varying local conditions. For the sake of brevity these results are not shown in the paper. To overcome this limitation, the current study adopts a new and more general approach, defining a vector quality metric as a modified signal-to-noise ratio $G(\tau)$,

$$G(x, y, t, \tau) = Q(x, y, t, \tau)\left(\frac{s_{mag}(x,y,t,\tau)}{\Delta s(x,y,t,\tau)}\right)^m \tag{2}$$

The optimal pulse separation $\tau_{opt}(x, y, t)$, based on the local maximum vector quality is given from $\max_\tau[G(\tau)]$. Note that $\tau_{opt}(x, y, t)$ is not a global but a *relative* optimum, determined by the greatest value of $G(\tau_i)$ from the finite number of chosen pulse separation times τ_i in a particular dataset. The criterion does not assume constant pixel displacement, and as such is applicable to time-resolved data. The calculation of G is based on the readily available correlation peak ratio and displacement magnitude but also requires determining the local uncertainty $\Delta s(x, y, t, \tau)$, which is described below. In this paper, an exponent $m = 4$ is chosen in Eq. (2). Values in the range $1 \leq m \leq 10$ shift the balance between correlation strength (low pulse separation) and relative displacement accuracy (higher pulse separation). The old vector quality metric Q' (Eq. (1)) could be adapted by replacing the global constant uncertainty estimate σ_s with the local estimate Δs (described below). However, the vector quality metric G (Eq. (2)) proved more robust and is more elegant in its definition as a combination of the correlation map signal-to-noise ratio Q and dynamic velocity range $s_{mag}/\Delta s$.

Performing a Reynolds decomposition on the PIV displacement field $s(x, y, t)$ yields

$$s(x, y, t) = \bar{s}(x, y) + s'(x, y, t) + \epsilon_s(x, y, t) + \beta_s(x, y, t) \tag{3}$$

where $\bar{s}(x, y)$ is the true time-averaged velocity and $s'(x, y, t)$ is the true turbulent velocity fluctuation, $\epsilon_s(x, y, t)$ is the random error and $\beta_s(x, y, t)$ is the bias error. Previous studies have used indirectly estimated error levels through mapping this relationship [23, 24], through quantifying the effect of errors on correlation space metrics [25, 26] or by using high-resolution image analysis [27]. The current study adopts a heuristic approach, calculating an estimate for $\Delta s = \sqrt{\epsilon_s^2 + \beta_s^2}$ as the rms deviation from the local displacement magnitude in a kernel of (n_x, n_y, n_t) adjacent vector grid locations in the spatiotemporal domain $[x, y, t]$, as shown in Fig. 1.

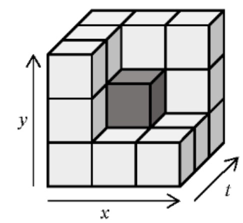

Figure 1. Local uncertainty estimation based on the RMS deviation in a kernel of size $(\boldsymbol{n_x}, \boldsymbol{n_y}, \boldsymbol{n_t})$.

The local magnitude is defined as the mean value of the kernel, $s_{mag}(x, y, t) = \frac{1}{n_x n_y n_t} \sum s(x, y, t)$. Instead of the more computationally efficient mean value, the median could be used to ignore outliers. The local uncertainty estimate is defined as

$$\Delta s(x, y, t) = \sqrt{\frac{1}{n_x n_y n_t} \sum \left[s(x, y, t) - s_{mag}(x, y, t)\right]^2} \tag{4}$$

Here, $n_x = n_y = 5$ and $n_t = 9$ (i.e., 225 elements), selected symmetrically around each vector grid location. For the sake of brevity it was not deemed appropriate to include a full parametric study of the effect on the HDR results for different values of m, n_x, n_y, n_t. In general, n_x and n_y should be greater than or equal to 3 to measure spatial fluctuations, yet be small enough to avoid excessive spatial smoothing. A similar balance holds for n_t, which should be kept small enough to avoid excessive temporal smoothing in the HDR results. If the value of n_t is chosen too large, the HDR algorithm will be less likely to pick different pulse separation values at consecutive time instants in a given spatial location. A larger kernel size $(n_x n_y n_t)$ also means a higher computational cost to determine $\Delta s(x, y, t)$. However the actual thresholds depend on the specific optical arrangement and flow conditions, making general recommendations difficult. For the kernel size and the exponent *m*, expert user judgment is still required as with any other PIV experiment.

Referring to Eq. (3), the expression in Eq. (4) returns a combination of physical turbulent fluctuations and measurement uncertainty (both random and bias error contributions). Only if the turbulent fluctuation s' can be considered invariable over τ_i and the bias error β_s assumed small, will Eq. (4) accurately estimate the random error ϵ_s.The bias error is a function of the fill ratio of the camera, the PIV algorithm used and the degree of peak locking due to sub-pixel sized tracer particles. Previous work has helped to quantify and minimize this error [28-30].

Although the uncertainty from Eq. (4) is contaminated by turbulent fluctuations and bias error, this should be of minor importance for the MPS algorithm. To determine the local optimal pulse separation, the values of $G(x, y, t, \tau_i)$ using Eq. (2) are compared *relative to each other* for all τ_i acquired in the *same flow field* with the *same optical arrangement and seeding conditions*.

By selecting a greater pulse separation $(\tau_{opt} \geq \tau_{min})$ in the low velocity region and a smaller pulse separation in the high velocity region, the minimum measurable velocity $\sigma_V \propto \sigma_s / \tau_{opt}$ and the dynamic velocity range increases by a factor $k_\tau = \tau_{opt}/\tau_{min}$ compared to conventional multi-grid PIV:

$$DR_V^{(MPS)} = \frac{\frac{1}{4} k_g d_I / \tau_{min}}{\sigma_s^{(MG)} / \tau_{opt}} = k_\tau k_g \frac{\frac{1}{4} d_I}{\sigma_s^{(MG)}} = k_\tau DR_V^{(MG)} \tag{5}$$

While the dynamic velocity range is increased by a factor k_τ, the dynamic spatial range ($\propto k_g d_I / \sigma_s^{(MG)}$) is not directly affected. These important dynamic ranges are therefore (at least partially) decoupled by this approach. In a practical experiment, the smallest pulse separation τ_{min} is chosen to limit the loss of correlation in regions of high velocity magnitude and shear, while the greatest pulse separation is chosen to give a measureable displacement magnitude in low velocity regions. The selection of the most suitable local pulse separation in the final HDR PIV flow field is determined solely by the relative maximum of the vector quality metric defined by Eq. (2).

III. Experimental Approach

A. Experimental Apparatus

As a benchmark case, an axisymmetric turbulent air jet is selected, issuing from a settling chamber with 75 mm internal diameter and flow straightener via a contoured nozzle with a radius of curvature of 10 mm and an exit diameter D = 5.0 mm, as depicted schematically in Fig. 2. Identified flow regions are (i) jet core, (ii) shear layer, (iii) outer shear layer, (iv) entrainment region). Indicated components of the jet facility are (a) compressor, filter and dryer, (b) pressure regulator valve and air flow meter, (c) settling chamber with flow conditioning and contoured nozzle, (d) PIV measurement region shown in Figs. 3-8, (e) hot-wire probe. Air is supplied from the building compressed air supply via an expansion valve and digital air mass flow meter (Alicat Scientific, Inc., 500 standard liters per minute, ±0.5% combined repeatability and accuracy). All experiments in the current paper are performed at Re = 9100 (mean jet nozzle velocity $U_{jet} \cong 27$ m/s). Glycol-water based aerosol seeding is introduced partly via a venturi in the air supply line and partly in the surrounding ambient air. The generated seeding droplets have a mean diameter between 0.2 and 0.3 μm and the particle images are 2 pixels in diameter. A high-repetition rate pulsed laser (Quantronix DarwinDuo double-pulsed Nd:YLF laser, 527nm, 15mJ at 2 kHz, 120ns pulse width) and a Photron Fastcam SA1 CMOS high-speed camera (1024^2 pixels, 5.4 kHz, 12 bit) are used for these experiments. A customized pulse timing system is available to apply different pulse separation values in successive pairs of frames, although for the experiments discussed in this paper, the simpler time-resolved double-frame approach is used as described in Section II. The laser sheet is adjusted to 0.5 mm thickness, coplanar with the jet centerline. The optical scaling factor is $M = 33$ μm/pixel.

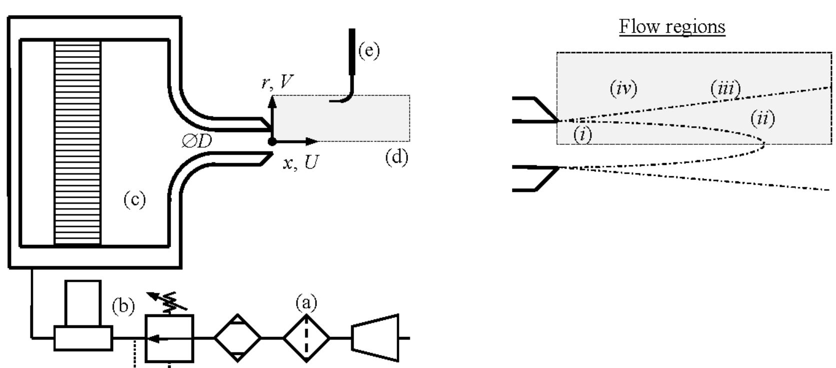

Figure 2. Schematic representation of the axisymmetric jet flow facility and jet flow regions.

As an independent velocity measurement, a single component right-angle hot wire probe (Dantec Dynamics 55P14, 1.25 mm long, 5 μm diameter platinum-plated tungsten) is used with a constant temperature anemometer (Dantec Dynamics 54T30 MiniCTA) in selected characteristic locations in the flow field. The HWA measurements are performed after the PIV measurements, without seeding particles but otherwise identical flow conditions. The probe is positioned in the PIV measurement plane using the camera to check its actual position, with the wire aligned perpendicular to the PIV plane (represented by (e) in Fig. 2). In each point, data is acquired for several seconds at 20 kHz. The hot wire was calibrated in the same jet flow using the mass flow meter as reference. King's law was least-square fitted to describe the voltage-velocity relationship between 1 m/s and 48 m/s ($R^2 > 0.99$, rms deviation 3%).

B. PIV Acquisition and Vector Evaluation

Double-frame images are acquired at 2920 Hz for 0.935 s corresponding to the maximum in-camera storage capacity. The pulse separation is set to $\tau_{min} = 10$ μs resulting in about 8 pixel displacement in the jet core region. This proved to be the maximum pulse separation without causing excessive loss of vectors in the shear layer as a result of the strong velocity gradients. Using the approach described in Section II, the HDR algorithm is applied with $\tau_{min} = 10$μs and $\tau_{max} = 1/(2920\text{Hz}) \cong 342$μs. Therefore, the maximum theoretical enhancement of the dynamic velocity range is 34.2 times. The dynamic velocity range will be discussed in more detail in Section IV.A, Tables 1 and 2, where it will be shown that the effective increase in dynamic velocity range is 16.5 times.

Vector evaluation is performed with Lavision DaVis 7.2.2, using a multi-grid cross-correlation algorithm with initial interrogation window size of 64^2 pixels (2 passes, 75% window overlap) and final interrogation window size of 32^2 pixels (2 passes, 75% window overlap) with Whittaker reconstruction applied in the final pass. The vector evaluation is verified with in-house developed code in Trinity College Dublin, using higher order peak detection methods. HDR reconstruction is performed in a post-processing step on the resulting vector fields, using in-house developed Matlab code implementing the equations described in Section II.

IV. Experimental Results and Discussion

The results presented in this paper are determined for the same axisymmetric unconfined air jet at Re = 9100 (D = 5.0 mm, mean jet nozzle velocity $U_{jet} \cong 27$ m/s). After verifying the symmetry of the flow field, only half plane flow fields are shown in this section ($0 \leq r/D \leq 2$ and $0 \leq x/D \leq 6$) for the sake of clarity.

A. Effect of HDR PIV on the Time-Averaged Flow Field Results

Figures 3 and 4 compare the PIV flow field measurements using conventional double-frame correlation at $\tau_{min} = 10$ µs (a, d); conventional time-series correlation at $\tau_{max} = 342$ µs (b, e); and the HDR PIV resulting from the combination of the above (c, f). All results shown in Figs. 3 and 4 are averaged over the maximum measurement duration of 0.935 s.

Figure 3(a-c) shows only a minor effect of using HDR PIV on the mean velocity magnitude, with a slightly smoother velocity contour line (at 0.02) in the entrainment region. However, Fig. 3(d-f) shows a significant reduction in measured turbulence intensity in the outer shear layer and entrainment region. The original conventional PIV results at $\tau_{min} = 10$ µs (Fig. 3d) exhibit a strong overestimation of turbulence intensity due to noisy low velocity vectors evaluated at the lower limit of the dynamic velocity range. The time-series PIV results for $\tau_{max} = 342$ µs (Fig. 3e) show more realistic low turbulence intensity in the entrainment region (0.2%-0.5%) yet fail

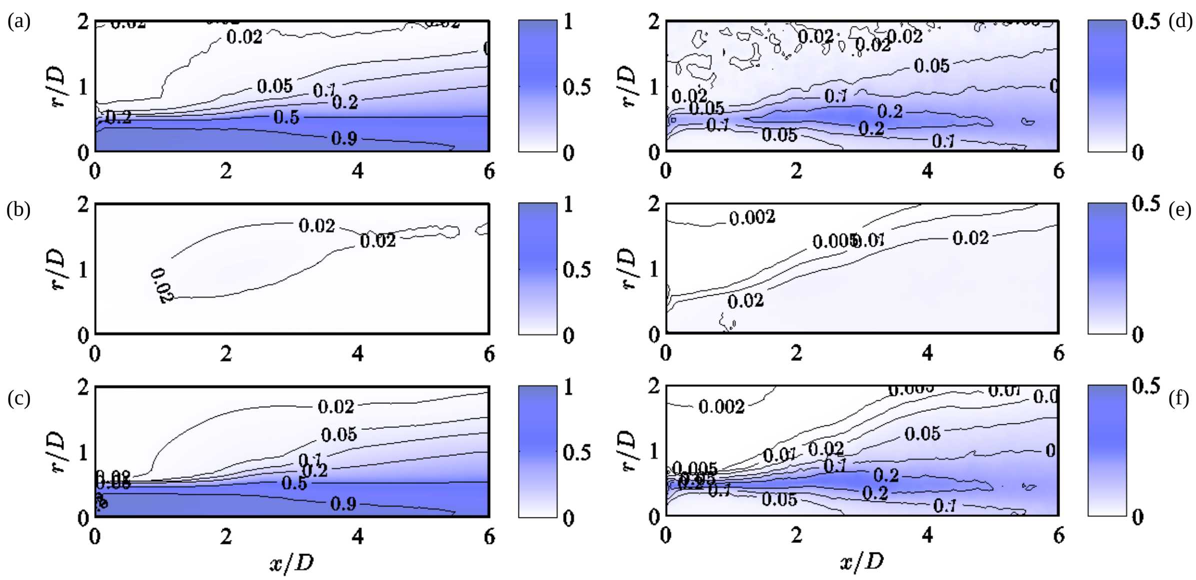

Figure 3. Time-averaged (a-c) velocity $\sqrt{U^2+V^2}/U_{jet}$ and (d-f) turbulence intensity $\sqrt{u'^2+v'^2}/U_{jet}$ using conventional PIV at (a, d) $\tau = \tau_{min}$, (b, e) $\tau = \tau_{max}$, and (c, f) HDR PIV at $\tau_{opt}(x, y, t)$.

to produce vectors in the central higher velocity region. The HDR turbulence field (Fig. 3f) seems to successfully combine the useful information from both vector evaluations into a wider dynamic range flow field.

Although in general, smoother streamlines and lower rms fluctuation intensities do not necessarily mean more accurate results, this is indeed the case for this specific well-studied flow field where the entrainment region is

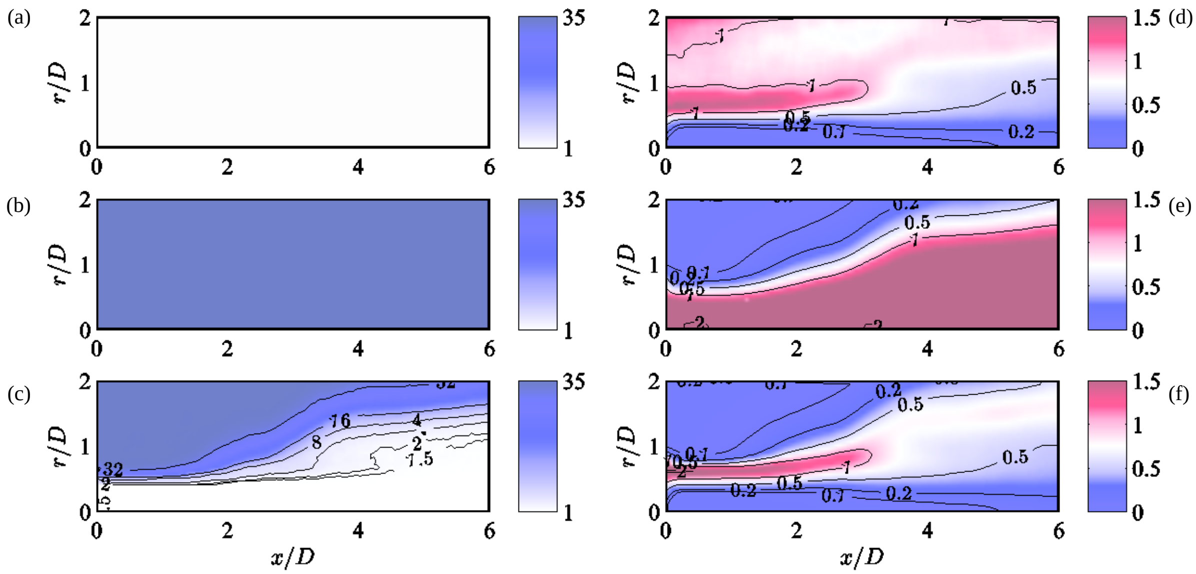

Figure 4. Time-averaged (a-c) pulse separation $\overline{\tau(x,y,t)/\tau_{min}}$ and (d-f) uncertainty $\overline{\Delta s/s_{mag}}$ using conventional PIV at (a, d) $\tau = \tau_{min}$, (b, e) $\tau = \tau_{max}$, and (c, f) HDR PIV at $\tau = \tau_{opt}(x,y,t)$.

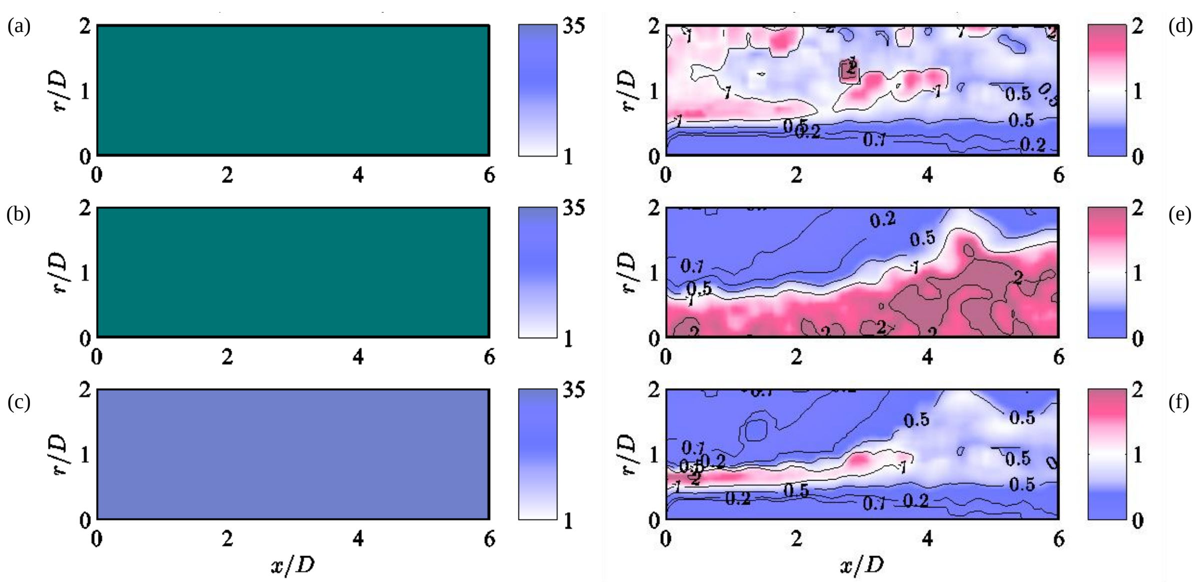

Figure 5. Instantaneous (a-c) pulse separation $\tau(x,y,t_0)/\tau_{min}$ and (d-f) uncertainty $\Delta s(x,y,t_0)/s_{mag}(x,y,t_0)$ for the same cases as Fig. 4.

Table 1. Overview of percentile values for the time-averaged velocity magnitude and uncertainty (Eq. (4)), pulse separation, and dynamic velocity range, for the cases in Figs. 3 and 4.

Cases (corresponding to Figs. 3 and 4)	**Velocity magnitude** $U_{mag} = s_{mag}/\tau$, m/s			**Velocity uncertainty** $\Delta U = \Delta s/\tau$, m/s			**Pulse separation** $k_\tau = \tau/\tau_{min}$			**Dynamic range** $DR_V \cong \frac{U_{mag}^{(99\%)}}{\Delta U^{(1\%)}}$
	(1%)	(50%)	(99%)	(1%)	(50%)	(99%)	(1%)	(50%)	(99%)	
(a, d) Conventional PIV with $\tau = \tau_{min}$	0.123	0.833	**25.5**	**0.29**	0.875	9.48	1	**1**	1	**88.3** ($\cong 10^{1.9}$)
(b, e) Conventional PIV with $\tau = \tau_{max}$	0.047	0.378	0.87	0.017	0.261	0.79	34.2	34.2	34.2	50.3 ($\cong 10^{1.5}$)
(c, f) HDR PIV with $\tau = \tau_{opt}(x, y, t)$	0.068	0.694	**25.5**	**0.017**	0.543	10.08	1.0	**2.68**	34.2	**1460.1** ($\cong 10^{3.1}$)

Table 2. Overview of percentile values for the instantaneous velocity magnitude and uncertainty (Eq. (4)), pulse separation, and dynamic velocity range, for the cases in Fig. 5.

Cases (corresponding to Fig. 5)	**Velocity magnitude** $U_{mag} = s_{mag}/\tau$, m/s			**Velocity uncertainty** $\Delta U = \Delta s/\tau$, m/s			**Pulse separation** $k_\tau = \tau/\tau_{min}$			**Dynamic range** $DR_V \cong \frac{U_{mag}^{(99\%)}}{\Delta U^{(1\%)}}$
	(1%)	(50%)	(99%)	(1%)	(50%)	(99%)	(1%)	(50%)	(99%)	
(a, d) Conventional PIV with $\tau = \tau_{min}$	0.111	0.814	**25.7**	**0.19**	0.778	9.64	1	**1**	1	**136.2** ($\cong 10^{2.1}$)
(b, e) Conventional PIV with $\tau = \tau_{max}$	0.043	0.364	0.91	0.013	0.250	0.86	34.2	34.2	34.2	68.2 ($\cong 10^{1.6}$)
(c, f) HDR PIV with $\tau = \tau_{opt}(x, y, t)$	0.066	0.692	**25.7**	**0.014**	0.460	9.89	1.0	**1.0**	34.2	**1879.8** ($\cong 10^{3.1}$)

known to exhibit near zero turbulence intensity laminar flow. For a confined impinging jet flow field at a similar Reynolds number, Persoons and O'Donovan [18] provided a direct comparison between non-time-resolved HDR PIV and laser-Doppler velocimetry results which has confirmed this. There may also be some undesirable smoothing present in the results due to the inherent spatial and temporal filtering effect caused by applying the HDR algorithm. This can be controlled by avoiding an excessively large kernel size to determine of Δs with Eq. (4).

Figure 4(a-c) shows the time-averaged pulse separation (normalized by τ_{min}) used for the results in Fig. 3. For the HDR results, a gradual transition is observed from 1 in the central high velocity region to $\tau_{max}/\tau_{min} \cong 34.2$ beyond the outer shear layer. For each vector in time and space, either the lowest or highest pulse separation vector is selected, as seen in Fig. 5(a-c) showing the corresponding distribution of the normalized pulse separation at one arbitrary time t_0.

Since the time-averaged transition is gradual with a range of intermediate values in the shear layer, the HDR algorithm does not always select the same pulse separation for a given location. Instead, it adapts to the local instantaneous vector evaluation conditions as determined by the value of the vector quality metric $G = Q\left(\Delta s/s_{mag}\right)^{-m}$ (Eq. (2)), with the estimated uncertainty Δs calculated for each vector from Eq. (4). Even though in this experiment there is a large difference between the two pulse separation values τ_{min} and τ_{max}, there is no discernible discontinuity in the velocity field in the region where the HDR algorithm selects either the smallest or largest pulse separation value, as demonstrated by the instantaneous velocity fields shown in Fig. 6f-j. No additional smoothing or any other post-processing of the resulting velocity field was carried out, other than selecting the optimum vector based on the maximum of $G(x, y, t, \tau)$ as defined in Eq. (2).

Figure 4(d-f) shows the time-averaged normalized uncertainty $\overline{\Delta s(x, y, t)/s_{mag}(x, y, t)}$, which takes quite high values in the entrainment region and outer shear layer near the nozzle for conventional PIV (Fig. 4d). This uncertainty $\Delta s/s_{mag}$, normalized with the *local* displacement magnitude, represents the inverse of the parameter which appears in the vector quality metric $G = Q\left(s_{mag}/\Delta s\right)^{m}$ (Eq. (2)), along with the correlation peak ratio Q. For $\tau = \tau_{max}$ (Fig. 4e) and the HDR results (Fig. 4f), the averaged relative uncertainty is much smaller in the same region. Only for the HDR results (Fig. 4f) with $\tau = \tau_{opt}(x, y, t)$, is the relative uncertainty smallest throughout the flow field. The most difficult region, also for HDR PIV, remains the shear layer near the orifice with its strong velocity gradients. It is worth reiterating that the high values of $\overline{\Delta s/s_{mag}}$ in Fig. 4f (up to 150% in the shear layer) are contaminated by strong physical velocity fluctuations in this region. As stated following the definition of Δs in Eq. (4), this metric is not intended to accurately represent the true uncertainty, yet is used merely in a comparative manner to determine the most suitable local pulse separation value.

The instantaneous results in Fig. 5(d-f) show a similar behavior, with the HDR method successfully avoiding vectors with excessive uncertainty in the entrainment and outer shear layer region, and replacing these with values from the high pulse separation evaluation. As noticed in the time-averaged results, the near-nozzle shear layer remains characterized by relative uncertainty values higher than unity; this could possibly be reduced by a different choice of pulse separation τ_{max}, or by using more than two pulse separation values in the HDR algorithm, which is beyond the scope of this study.

Tables 1 and 2 summarize some relevant statistics for the results presented in Figs. 3-5. The time-averaged results are presented in Table 1 (corresponding to Figs. 3 and 4), while Table 2 presents the instantaneous results for $t = t_0$ (corresponding to Fig. 5). Each set of 3 values represents the 1st, 50th (median) and 99th percentile values throughout the entire spatial field ($0 \le r/D \le 2$ and $0 \le x/D \le 6$). Percentiles are used to disregard the top and bottom 1% outliers. The local velocity magnitude is defined as $U_{mag}(x,y,t) = s_{mag}(x,y,t)/\tau(x,y,t)$ (given in m/s) and similarly for the velocity uncertainty $\Delta U(x,y,t) = \Delta s(x,y,t)/\tau(x,y,t)$. Velocity values are given instead of displacement because the final column gives an estimate of the dynamic velocity range for each case, defined as

$$DR_V \cong \frac{U_{mag}^{(99\%)}}{\Delta U^{(1\%)}} \tag{6}$$

where $U_{mag}^{(99\%)}$ represents the 99th percentile of the local velocity magnitude, and $\Delta U^{(1\%)}$ represents the 1st percentile of the local velocity uncertainty, where Δs is determined according to Eq. (4). The definition is Eq. (6) is used to estimate the actual dynamic velocity range in each flow field evaluation, since the local magnitude and uncertainty from Eq. (4) can be considered reasonable estimates for the maximum and minimum resolvable velocity. As mentioned above, the 1st and 99th percentiles disregard outliers at both ends of the range which likely results in a more realistic estimate of the dynamic velocity range. Equation (6) offers a more direct way of calculating the dynamic velocity range compared to the more indirect definition for DR_V in Eq. (5) relying on pulse separation values, which was used previously by the author [31] but which could easily overestimate the true dynamic velocity range. As discussed in Section II, the uncertainty Δs from Eq. (4) is contaminated with both physical fluctuations and bias error. Thus, the main outcome of the values in Tables 1 and 2 should be the *relative* increase of DR_V when using HDR PIV compared to conventional PIV, not the absolute values. For the time-averaged results, the dynamic velocity range (from Eq. (6)) increases by a factor of $1460/88.3 = 16.5$ times, or 1.2 orders of magnitude.

B. Effect of HDR PIV on the Time-Resolved Flow Field Results

Figure 6 shows a time sequence of the vorticity field using conventional PIV ($\tau = \tau_{min}$) on the left hand side, and HDR PIV on the right hand side for five consecutive times $t_0 + [0, \delta t, 2\delta t, 3\delta t, 4\delta t]$, where t_0 is the same arbitrarily chosen time used in Fig. 5 and Table 2. Instantaneous streamlines are superimposed to highlight the poor dynamic range of conventional PIV which is particularly obvious in the entrainment region due to the low velocity magnitude there. The HDR results in Fig. 6(f-j) show a quasi-seamless transition from smooth streamlines in the low velocity regions to the high velocity turbulent jet flow, at each instant in time.

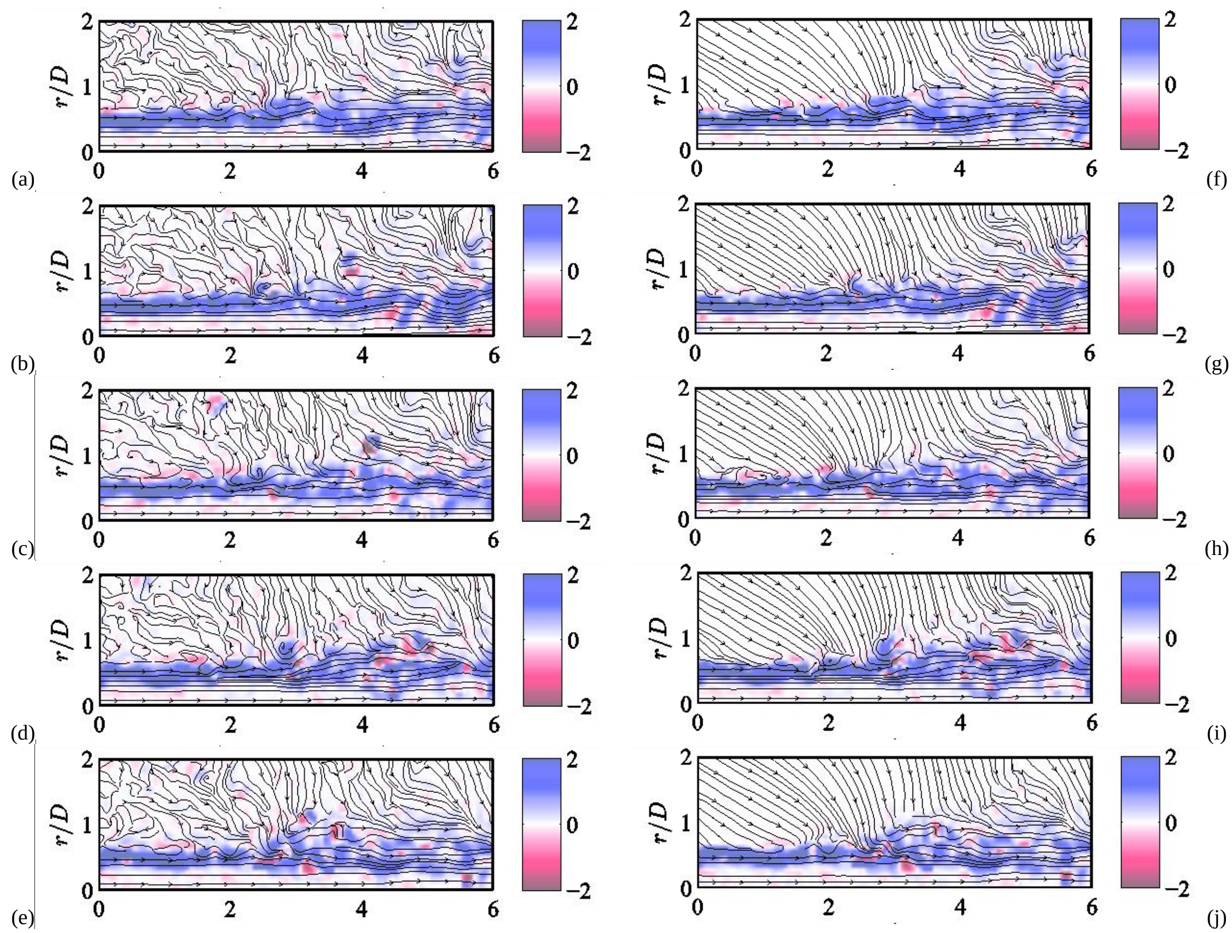

Figure 6. Time-resolved sequence (top to bottom) of streamlines and vorticity $\omega(x, y, t)D/U_{jet}$ in steps of $\delta t = 0.3425$ ms: (a-e) conventional PIV ($\tau = \tau_{min}$) and (f-j) HDR PIV ($\tau = \tau_{opt}(x, y, t)$).

Figures 7 and 8 show time and frequency domain plots of the measured velocity in a few characteristic locations, where hot-wire anemometry (HWA) measurements were also taken in the same flow field yet without seeding. The measurements were not carried out simultaneously and the comparison between HWA and local PIV results in Figs. 7-8 is made only in terms of velocity characteristics such as the time-averaged mean and fluctuation velocity, the velocity probability density function shown to the right of each time trace, and the frequency spectrum. The spatial locations were chosen in the middle of the jet core region (Fig. 7a,b), in the far shear layer (Fig. 7c,d), in the entrainment region (Fig. 8a,b) and in the outer shear layer (Fig. 8c,d). The locations used in Figs. 7 and 8(a,b) correspond to the exact location of the hot wire probe as determined in the camera image, while no HWA readings were available in the location shown in Fig. 8(c,d).

The HWA readings were acquired at 20 kHz while the PIV recording was done at 2.92 kHz, hence the difference in the frequency domain range for the signals. In Fig. 7(a,b), the HWA velocity shows evidence of harmonic

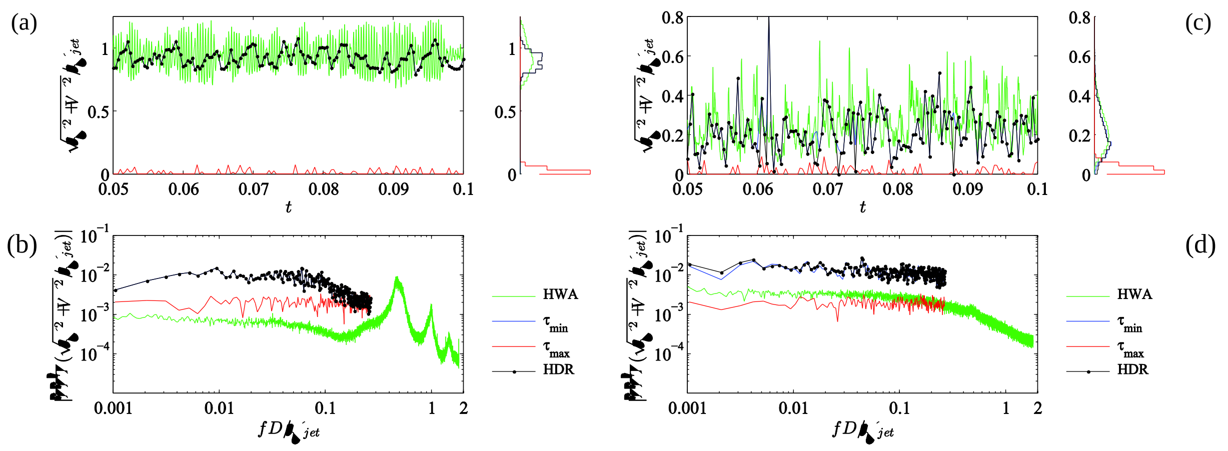

Figure 7. Velocity $\sqrt{U^2+V^2}/U_{jet}$ at (a, b) $[x,r] \cong [3.0, 0.1]D$ and (c, d) $[x,r] \cong [4.5, 0.8]D$: (—) hot-wire anemometer, conventional PIV with (—) $\tau = \tau_{min}$, (—) $\tau = \tau_{max}$, and (–•–) HDR PIV with $\tau = \tau_{opt}(x,y,t)$.

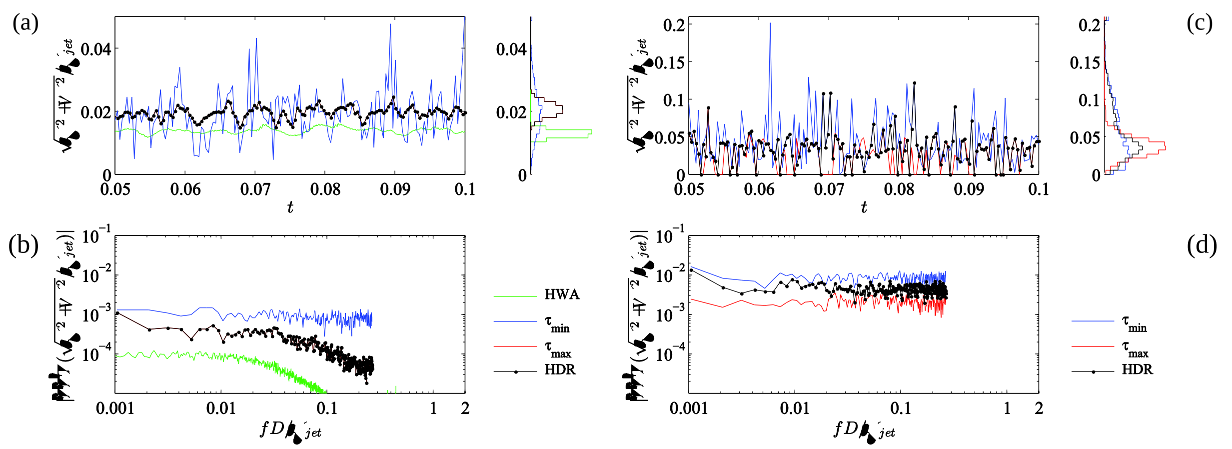

Figure 8. Velocity $\sqrt{U^2+V^2}/U_{jet}$ at (a, b) $[x,r] \cong [1.5, 1.1]D$ and (c, d) $[x,r] \cong [3.0, 1.1]D$: (—) hot-wire anemometer, conventional PIV with (—) $\tau = \tau_{min}$, (—) $\tau = \tau_{max}$, and (–•–) HDR PIV with $\tau = \tau_{opt}(x,y,t)$.

oscillations of the same order of magnitude as the natural vortex shedding frequency of the jet. Because the PIV recording rate is lower than the shedding frequency for this jet flow, the same oscillations are not picked up in the PIV results, which explains the difference in fluctuation amplitude shown in the time trace and the probability density function (pdf) shown on the right hand side of Fig. 7(a). These harmonic oscillations are less pronounced in the far shear layer location (Fig. 7c,d) and here, the HDR PIV and HWA results are in reasonably good agreement. It is worth noting that the HWA and PIV signals were not acquired simultaneously, so the comparison should not be based on instantaneous readings in time, but only on the pdf distribution and frequency spectrum. Comparing the conventional and HDR PIV results, Fig. 7(a,b) at location $[x,r] \cong [3.0,0.1]D$ shows that the HDR results completely overlap the results for $\tau = \tau_{min}$ since no valid vectors were determined at the higher pulse separation at that location in the jet core region. A similar situation is observed in Fig. 7(c,d) in the far shear layer ($[x,r] \cong [4.5,0.8]D$).

Figure 8(a,b) shows the HDR algorithm giving preference to the higher pulse separation vectors in the entrainment region ($[x,r] \cong [1.5,1.1]D$) since the dynamic velocity range is enhanced in this low mean velocity region. Here, the HWA results are lower in magnitude although the fluctuation intensity and the general shape of the frequency spectrum are in reasonable agreement with the HDR PIV results. The PIV data obtained with the smallest pulse separation fails to capture the decreasing trend in the frequency spectrum for $fD/U_{jet} > 0.025$ in Fig. 8(a.b). The HDR PIV is in better agreement with the HWA spectrum. The reason for the deviation could be a combination of a limited calibration velocity range (1-48 m/s) and the oblique flow in this region, with local flow angles up to 30° from the centerline which the single-wire HWA probe is not capable of resolving accurately.

Figure 8(c,d) compares the PIV results in a location in the outer shear layer ($[x,r] \cong [3.0,1.1]D$) where unfortunately no HWA measurements were taken at the time of the experiments. In this location, the time trace shows the HDR PIV velocity switching between the low and high pulse separation data, maximizing the vector quality for each time record. A similar behavior is observed in a broad region as represented by intermediate normalized pulse separation values $\overline{\tau(x,y,t)/\tau_{min}}$ between 1.5 and 32 in Fig. 4(c), roughly corresponding to the outer shear layer.

C. Limitations of the Multiple Pulse Separation HDR Technique

In the experimental results discussed above, the simplest approach was used in combining the information from two different pulse separation time values, requiring no customized or additional hardware and minimal additional processing. Using a conventional double-pulsed time-resolved PIV system, the time between consecutive laser pulses A and B is τ_{min} and the first displacement field $\vec{s}(\tau_{min})$ is evaluated using double-frame correlation of $[I(t), I(t+\tau)]$. The laser repetition rate $(1/\delta t)$ determines $\tau_{max}(= \delta t)$ and the second displacement field $\vec{s}(\tau_{max})$ is evaluated using time-series correlation of $[I(t), I(t+\delta t)]$. Both displacement fields are obtained at time instants $t + \frac{1}{2}\tau$ and $t + \frac{1}{2}\delta t$, or a temporal difference equal to $\frac{1}{2}(\delta t - \tau)$ ($\cong$ 166 μs in this case). To avoid this ambiguity a straddling method could be used, with time-series correlation of $[I(t - \delta t + \tau), I(t + \delta t)]$ to obtain $\vec{s}(\tau_{max})$, resulting in zero time difference (with $\tau_{max} = 2\delta t - \tau$). However, for the purpose of demonstrating the HDR technique in this paper, the temporal ambiguity was ignored. This is a reasonable approach as long as only spatial distributions of mean flow and turbulent fluctuation intensities are of interest.

As discussed in the introduction, multiple pulse separation and other multi-frame and multi-PIV pulse techniques aim to decouple the dynamic spatial range and dynamic velocity range, the product of which is constant for traditional double-pulsed systems [11, 12]. By locally adapting the pulse separation time to the flow field conditions, a high spatial resolution (i.e., small particle displacement compared to the image sensor size) can be combined with high velocity accuracy. However, this is likely an optimistic representation since the application of local variations in pulse separation time also entails variations in temporal smoothing and truncation errors in the presence of temporal acceleration and spatial acceleration, respectively [11]. In future, a combination of the present approach with new methods such as the triple-pulse PIV approach analyzed by Westerweel et al. [11] might be considered.

Finally, as with other methods where the pulse separation time is increased, care should be taken in interpreting the results obtained with this technique. Firstly, excessive loss of correlation (e.g., due to out-of-plane motion) may be an issue in strong turbulent flows if the pulse separation time becomes too large. However, by incorporating the correlation peak ratio directly in the vector quality metric, the proposed HDR PIV technique tends to select smaller pulse separation values in such adverse conditions. As shown in Figs. 4c and 5c, the favors the smaller pulse separation value in much of the outer turbulent shear layer, where out-of-plane motion is likely of the same order of magnitude as in-plane motion. No additional user intervention is required to accomplish this. Secondly, truncation errors due to a misrepresentation of the actual flow curvature increase with increasing pulse separation time [11, 13, 16, 17]. However since regions of strong fluid trajectory curvature are characterized by strong in-plane gradients which also indirectly affect the correlation peak ratio, the algorithm will tend to favor smaller pulse separation times in those conditions.

V. Conclusion

In this paper, the multiple-pulse-separation (MPS) technique for high dynamic range (HDR) PIV previously developed for steady and periodic flows [18] has been successfully extended towards *time-resolved* measurements. As a benchmark case, a high-repetition rate pulsed laser and camera system are used in combination with an axisymmetric turbulent air jet flow at Re = 9100 (D = 5.0 mm).

In order to implement the time-resolved HDR PIV technique, the method developed previously for non-time-resolved PIV [18, 19] has been modified into a new criterion for the local optimal pulse separation. This criterion is based on a new vector quality metric G (see Eq. (2)) comprising the correlation peak ratio Q and the estimated local relative displacement uncertainty as $s_{mag}/\Delta s$.

The HDR method automatically selects the most suitable local pulse separation and corresponding vector as a function of space and time, by maximizing the vector quality metric $\max_{\tau}[G(\tau)]$. The user-defined parameters include the size of the kernel in Eq. (4) and the exponent m in Eq. (2), which is set at $m = 4$ in this paper. Values for m between 1 and 10 shift the balance in the criterion between correlation strength Q and relative displacement accuracy $s_{mag}/\Delta s$, however the criterion is robust enough to avoid invalid vectors determined at excessive pulse separations. The chosen kernel size for the results presented in this paper is $5 \times 5 \times 9$ ($n_x = n_y = 5$ and $n_t = 9$), which is a compromise between calculation time and the desired spatiotemporal resolution of the magnitude and rms deviation metrics. Care should be taken to avoid unnecessary smoothing of the HDR results by keeping the kernel size small enough, although thresholds are application-dependent.

The most significant improvement of using HDR PIV was observed in the turbulence intensity fields in the entrainment and outer shear layer regions. Based on the ratio of pulse separation values, the maximum theoretical increase in dynamic velocity range is 34.2 times. The effective increase in dynamic velocity range in this flow field was calculated to be 16.5 times (1.2 orders of magnitude), from an estimated value of $DR_V \cong 88{:}1$ for conventional double-pulsed PIV to $DR_V \cong 1460{:}1$ for HDR PIV. Although this may be an optimistic estimate (neglecting the effect of the increase in temporal and spatial acceleration), it brings the dynamic velocity range closer to the targeted value of 1000:1 put forward by Westerweel et al. [11].

Comparing the PIV data to hot-wire anemometry (HWA), the HDR PIV results perform somewhat better in capturing the trends in the frequency spectrum in selected locations in the entrainment region. However, even the HDR PIV data consistently overestimate the turbulent fluctuation intensity compared to the HWA measurement.

HDR PIV has its limitations (see Section IV.C) and expert judgment remains required to assess its validity. Care should be taken in choosing the minimum and maximum pulse separation, similar to traditional double-pulsed PIV experiments. However, the method is implemented entirely based on readily available data. It has a low computational cost and since it is implemented as a post-processing routine, it is fully compatible with all conventional multi-grid vector evaluation algorithms, such as those implemented in commercial PIV software packages.

Acknowledgments

The author thanks Mr Rudi O'Reilly Meehan for the assistance with the HDR PIV data processing, and Prof Darina B. Murray for the use of the particle image velocimetry equipment.

References

[1]Keane, R. D., and Adrian, R. J., "Optimization of Particle Image Velocimeters. 1. Double Pulsed Systems," *Measurement Science and Technology*, Vol. 1, No. 11, 1990, pp. 1202-1215.

[2]Keane, R. D., and Adrian, R. J., "Theory of Cross-Correlation Analysis of PIV Images," *Applied Scientific Research*, Vol. 49, No. 3, 1992, pp. 191-215.

[3]Raffel, M., Willert, C. E., Wereley, S. T., and Kompenhans, J., *Particle Image Velocimetry: A Practical Guide*, 2nd ed., Springer-Verlag, Berlin, Germany, 2007, pp. 164-176.

[4]Westerweel, J., "Fundamentals of Digital Particle Image Velocimetry," *Measurement Science and Technology*, Vol. 8, No. 12, 1997, pp. 1379-1392.

[5]Westerweel, J., "On Velocity Gradients in PIV Interrogation," *Experiments in Fluids*, Vol. 44, No. 5, 2008, pp. 831-842.

[6]Westerweel, J., Dabiri, D., and Gharib, M., "The Effect of a Discrete Window Offset on the Accuracy of Cross-Correlation Analysis of Digital PIV Recordings," *Experiments in Fluids*, Vol. 23, No. 1, 1997, pp. 20-28.

[7]Scarano, F., "Iterative Image Deformation Methods in PIV," *Measurement Science and Technology*, Vol. 13, No. 1, 2002, pp. R1-R19.

[8]Scarano, F., and Riethmuller, M. L., "Advances in Iterative Multigrid PIV Image Processing," *Experiments in Fluids*, Vol. 29 (Suppl.), 2000, pp. S51-S60.

[9]Scarano, F., and Riethmuller, M. L., "Iterative Multigrid Approach in PIV Image Processing with Discrete Window Offset," *Experiments in Fluids*, Vol. 26, No. 6, 1999, pp. 513-523.

[10]Stanislas, M., Okamoto, K., Kähler, C. J., and Westerweel, J., "Main Results of the Second International PIV Challenge," *Experiments in Fluids*, Vol. 39, No. 2, 2005, pp. 170-191.

[11]Westerweel, J., Elsinga, G. E., and Adrian, R. J., "Particle Image Velocimetry for Complex and Turbulent Flows," *Annual Review of Fluid Mechanics*, Vol. 45, pp. 409-436, 2013

[12]Adrian, R. J., "Dynamic Ranges of Velocity and Spatial Resolution of Particle Image Velocimetry," *Measurement Science and Technology*, Vol. 8, pp. 1393-1398, 1997

[13]Hain, R., and Kähler, C. J., "Fundamentals of Multiframe Particle Image Velocimetry (PIV)," *Experiments in Fluids*, Vol. 42, No. 4, 2007, pp. 575-587.

[14]Fincham, A., and Delerce, G., "Advanced Optimization of Correlation Imaging Velocimetry Algorithms," *Experiments in Fluids*, Vol. 29 (Suppl.), 2000, pp. S13-S22.

[15]Pereira, F., Ciarravano, A., Romano, G. P., and Di Felice, F., "Adaptive Multi-Frame PIV," *Proceedings of the 12th International Symposium on Applications of Laser Techniques to Fluid Mechanics*, Lisbon, Portugal, July 12-15, 2004

[16]Sciacchitano, A., Scarano, F., and Wieneke, B., "Multi-Frame Pyramid Correlation for Time-Resolved PIV," *Experiments in Fluids*, Vol. 53, No. 4, pp. 1087-1105, 2012

[17]Lynch, K., and Scarano, F., "A High-Order Time-Accurate Interrogation Method for Time-Resolved PIV," *Measurement Science and Technology*, Vol. 24, No. 3, Art.No. 035305, 2013

[18]Persoons, T., and O'Donovan, T. S., "High Dynamic Velocity Range Particle Image Velocimetry using Multiple Pulse Separation Imaging," *Sensors*, Vol. 11, No. 1, 2010, pp. 1-18.

[19]Persoons, T., Farrelly, R., McGuinn, A., and Murray, D. B., "High Dynamic Range Whole-Field Turbulence Measurements in Impinging Synthetic Jets for Heat Transfer Applications," *Proceedings of the 12th International Symposium on Applications of Laser Techniques to Fluid Mechanics*, Lisbon, Portugal, July 5-8, 2010.

[20]Battiato, S., Castorina, A., and Mancuso, M., "High Dynamic Range Imaging for Digital Still Camera: An Overview," *Journal of Electronic Imaging*, Vol. 12, No. 3, 2003, pp. 459-469.

[21]Mann, S., and Picard, R. W., "On Being 'Undigital' with Digital Cameras: Extending Dynamic Range by Combining Differently Exposed Pictures," *Proceedings of the IS&T Annual Conference on Imaging on the Information Superhighway*, Washington, DC, May 7-11, 1995, pp. 442-448.

[22]Reinhard, E., Ward, G., Pattanaik, S., and Debevec, P., *High Dynamic Range Imaging: Acquisition, Display, and Image-Based Lighting*, Morgan Kaufmann Publishers Inc., San Francisco, CA, 2005.

[23]Wilson, B. M., and Smith, B. L., "Uncertainty on PIV Mean and Fluctuating Velocity due to Bias and Random Errors," *Measurement Science and Technology*, Vol. 24, No. 3, 2013, Art.No. 035302.

[24]Timmins, B. H., Wilson, B. W., Smith, B. L., and Vlachos, P. P., "A Method for Automatic Estimation of Instantaneous Local Uncertainty in Particle Image Velocimetry Measurements," *Experiments in Fluids*, Vol. 53, No. 4, 2012, pp. 1133-1147.

[25]Charonko, J. J., and Vlachos, P. P., "Estimation of Uncertainty Bounds for Individual Particle Image Velocimetry Measurements from Cross-Correlation Peak Ratio," *Measurement Science and Technology*, Vol. 24, No. 6, 2013, Art.No. 065301.

[26]Xue, Z., Charonko, J. J., and Vlachos, P. P., "Particle Image Velocimetry Correlation Signal-to-Noise Ratio Metrics and Measurement Uncertainty Quantification," *Measurement Science and Technology* (in press), Preprint available on Cornell University Library, arXiv:1405.3023 (http://arxiv.org/abs/1405.3023, accessed May 26, 2014).

[27]Sciacchitano, A., Wieneke, B., and Scarano, F., "PIV Uncertainty Quantification by Image Matching," *Measurement Science and Technology*, Vol. 24, No. 4, 2013, Art.No. 045302.

[28]Huang, H., Dabiri, D., and Gharib, M., "On Errors of Digital Particle Image Velocimetry," *Measurement Science and Technology*, Vol. 8, No. 12, 1997, pp. 1427-1440.

[29]Nogueira, J., Lecuona, A., Nauri, S., Legrand, M., and Rodriguez, P. A., "Quantitative Evaluation of PIV Peak Locking Through a Multiple Delta t Strategy: Relevance of the RMS Component," *Experiments in Fluids*, Vol. 51, No. 3, 2011, pp. 785-793.

[30]Wereley, S. T., Gui, L., and Meinhart, C. D., "Advanced Algorithms for Microscale Particle Image Velocimetry," *AIAA Journal*, Vol. 40, No. 6, 2002, pp. 1047-1055.

[31]Persoons, T., "High Dynamic Range Particle Image Velocimetry Applied to Heat Convection Studies," *EPJ Web of Conferences*, Vol. 67, 2014, Art.No. 01001.